ChemCatChem

The European Society Journal for Catalysis

Chemistry Europe

European Chemical Societies Publishing

Supported by GECATS GERMAN CATALYSIS SOCIETY

Accepted Article

Title: Indium Phosphide Quantum Dots Integrated with Cadmium Sulfide Nanorods for Photocatalytic Carbon Dioxide Reduction

Authors: Kahi H. Do, D. Praveen Kumar, A. Putta Rangappa, Yul Hong, D. Amaranatha Reddy, and Tae Kyu Kim

To be cited as: *ChemCatChem* 10.1002/cctc.202000616

Link to VoR: https://doi.org/10.1002/cctc.202000616

WILEY-VCH

10.1002/cctc.202000616

WILEY-VCH

FULL PAPER

Indium Phosphide Quantum Dots Integrated with Cadmium Sulfide Nanorods for Photocatalytic Carbon Dioxide Reduction

Khai H. Do,[†[a]] Dr. D. Praveen Kumar,[†[a]] A. Putta Rangappa,[[a]] Yul Hong,[[a]] Dr. D. Amaranatha Reddy[[a]] and Prof. Tae Kyu Kim*[[a]]

[a] Department of Chemistry, Yonsei University, Seoul 03722, Republic of Korea
† These authors contributed equally.
E-mail: tkkim@yonsei.ac.kr

Supporting information for this article is given via a link at the end of the document

Abstract: Photocatalytic conversion of CO_2 into storable fuels is an attractive way to simultaneously address worldwide energy demands and environmental problems. Semiconductor quantum dots (QDs) have gained prominence as candidates for photocatalytic applications due to their many advantages, which include turnability for advanced electronic, optical, and surface properties. Indium phosphide (InP) quantum dots are semiconducting QDs with enormous potential for solar-driven CO_2 reduction. Their advantages include a tunable bandgap, diverse surface chemistry, and nontoxicity. InP QDs and CdS nanorods were integrated using a simple and inexpensive method. CO_2 photoreduction by the CdS-InP composites was evaluated in aqueous solution using triethanolamine as a sacrificial donor. The crystal structures, surface compositions, and morphologies were investigated via X-ray diffraction analysis, X-ray photoelectron spectroscopy, and transmission electron microscopy, respectively. The UV-visible diffuse reflectance spectra of the CdS-InP composites indicated efficient visible light utilization in the 500–550 nm range. The results of photoelectrochemical and photoluminescence analyses illustrated effective charge separation in the composites. The photocatalytic activity of the as-synthesized composites was superior to that of pure CdS. The CO evolution rate of the optimized composite was 216 μmol h^{-1} g^{-1} during the first three hours of irradiation and increased steadily over the next 62 hours. We also studied the influences of different solvents, the hole scavenger concentration, and catalyst loading on the optimized composite.

Introduction

The uncontrolled consumption of natural resources is depleting fossil fuel reserves, and combustion emissions are associated with serious environmental degradation. The development of eco-friendly and renewable wind and solar energy sources is essential to solve these problems. To this end, the development of solar fuels by using sunlight has become a foremost research goal. The photocatalytic conversion of CO_2 into value-added fuels is an environmentally-friendly, economical, and sustainable strategy for addressing the global energy demands and environmental issues. This is because the sun is the ultimate energy source, and water and CO_2 in industrial emissions are abundant.[1–3] There are many reports of using individual photocatalysts to convert CO_2 into value-added chemicals. However, developing economical high-performance photocatalysts for CO_2 conversion is an ongoing challenge.

Cadmium sulfide (CdS) is responsive to visible light, and it has attracted a great deal of attention as a semiconductor photocatalyst. It has a narrow bandgap (~2.4 eV), and its conduction band edge position is more negative than the reduction potential of CO_2.[4–6] However, the photoconversion efficiency of bare CdS is low due to its high charge carrier recombination rate and susceptibility to photocorrosion.[7–10] Loading the surface of CdS with another semiconductor or a co-catalyst to enhance photocatalytic activity has been a successful strategy. The combination of two or more materials can facilitate photogenerated charges carrier separation, expand the light absorption window, and improve visible light utilization.[11–13] The high photocatalytic efficiency of CdS mixed with noble metal (Pt, Ru, Pd, Ag) nanostructures has made these materials a top priority in the field of photocatalytic CO_2 reduction.[14–16] However, the high cost of manufacturing them on an industrial scale and the low abundance of noble metals are obstacles to the practical application and commercialization of these photocatalysts. A variety of CdS co-catalysts based on metal oxides,[17–19] carbon,[20,21] metal sulfide,[5,22] and ZIF[23,24] have been designed in an effort to overcome these limitations. Nevertheless, the instability of these co-catalysts during photocatalytic reactions is a major drawback.

Metal phosphides (MPs) have recently received significant interest in the field of photocatalysis on account of their abundance, good stability, low cost, and high electrical conductivity. These MPs include Co_xP,[25–28] Ni_2P,[29] Fe_2P,[30] Cu_3P,[31] and WP.[32] Due to the large atomic radius and the strong charge (−3) of phosphorus, the M–P bonds in most metal phosphides have a highly covalent character.[33–35] The presence of P moderates the bonding strength of metal phosphides towards photocatalytic conversion products, which facilitates the desorption of conversion products from active sites.[36,37] Despite having suitable physical and chemical properties, including high electron mobility,[38] indium phosphide (InP) semiconductors have not been thoroughly studied for photocatalytic CO_2 reduction.[39] The main obstacle to the widespread use of InP for photocatalysis is the large bulk bandgap (1.35 eV). However, this can be overcome by reducing the size of InP particles to the quantum dot (QD) scale. QDs, which are semiconductor nanocrystals, have unique size-dependent electronic and optical properties as well as versatile surface features. They have become prominent candidates for numerous applications, including light-emitting diodes (LEDs),[40,41] solar energy conversion,[42] and photocatalysis.[43–45] QDs based on cadmium chalcogenides have similar emission characteristics, low toxicity, and their fabrication is cost-effective.[46] InP should be considered as an alternative to cadmium chalcogenide-based materials, because the large bulk bandgap (1.35 eV) and Bohr exciton radius (9.6 eV) can be great

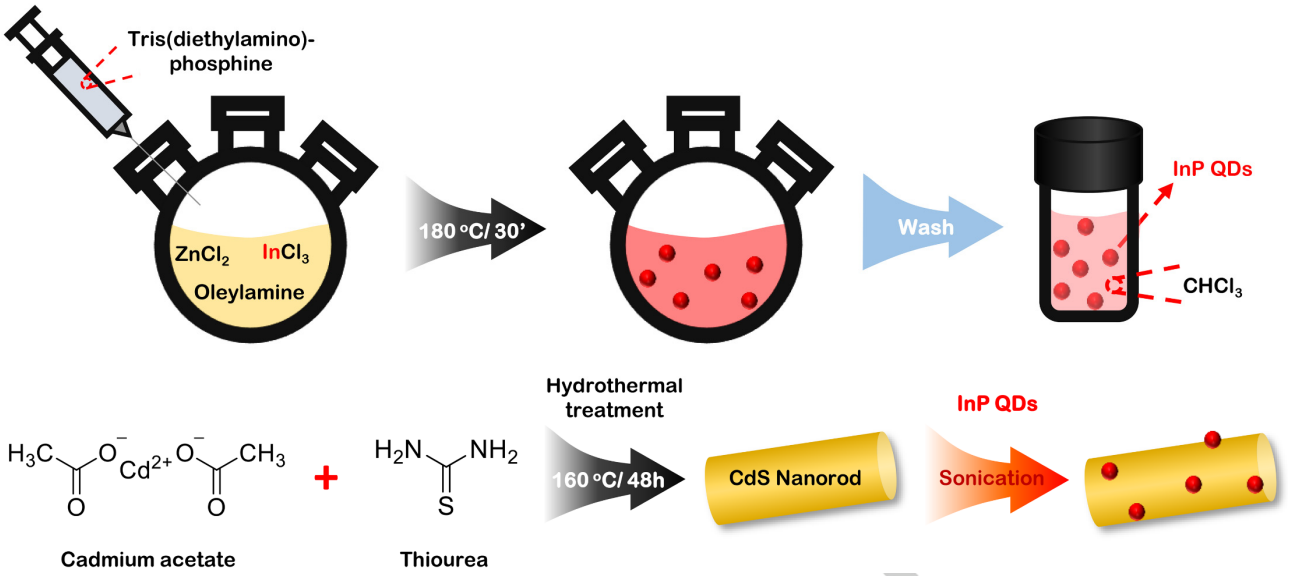

Scheme 1. Schematic illustration of material preparation of CdS NRs, InP QDs and CdS-InP composites

advantages for solar energy utilization by tuning the size of InP QDs. Additionally, InP QDs have higher redox potential than the bulk InP, which is favorable to photocatalytic reactions. Since photocatalytic reactions often occur at the interface between a semiconductor and co-catalyst, zero-dimensional InP QDs could provide more active sites for photocatalytic reactions than bulk InP. This would enhance photocatalytic activity at the semiconductor/InP heterojunction under visible light. A recent study reported on InP QDs and InP QD/semiconductors for solar-driven hydrogen production,[47] although the exploration of InP QDs for photocatalytic CO_2 reduction to produce value-added chemicals has been limited. InP/CdS-based core/shell QDs have been shown to be quasi- or type II heterostructures,[48,49] which are suitable for solar energy conversion. CdS integrated with InP QDs is thus expected to be a promising photocatalyst candidate.

Herein, we report the simple preparation of InP QDs and their integration with CdS nanorods (NRs) (CdS-InP nanocomposites). The synthesized materials were evaluated for the photocatalytic reduction of CO_2 in water under simulated solar light using triethanolamine as a sacrificial donor. The optimized CdS-InP composite demonstrated high CO_2 conversion efficiency, and its CO evolution rate (216 μmol h^{-1} g^{-1}) was 2.4 times higher than that of bare CdS during the first three hours of irradiation. The enhanced photocatalytic performance of these catalysts under simulated sunlight illumination was attributed to efficient charge carrier separation and the efficient utilization of visible light in the 500–550 nm range.

Results and Discussion

InP QDs were prepared by reacting $InCl_3$ and tris(diethylamino)phosphine in oleylamine. Oleylamine served as a coordinating solvent and played an integral role throughout the chemical process.[46,50,51] The presence of $ZnCl_2$ facilitated shell growth and reduced variability in the size of the InP QDs. This approach has been shown to prevent the formation of Zn-doped InP core nanocrystals.[46,50,52] We also added toluene in the procedure for azeotropic distillation. $ZnCl_2$ and $InCl_3$ absorbed water moisture, which could react with $ZnCl_2$ to form ZnO. Adding toluene and slowly increasing the temperature during evacuation helped prevent this (Figure S1a, Supporting Information). The dissolution-precipitation technique was utilized to remove the impurities, such as excess amounts of oleylamine and unreacted precursors. In addition, $ZnCl_2$ and $InCl_3$ were eliminated due to high solubility in ethanol. A Schematic illustration of material preparation showed in Scheme 1.

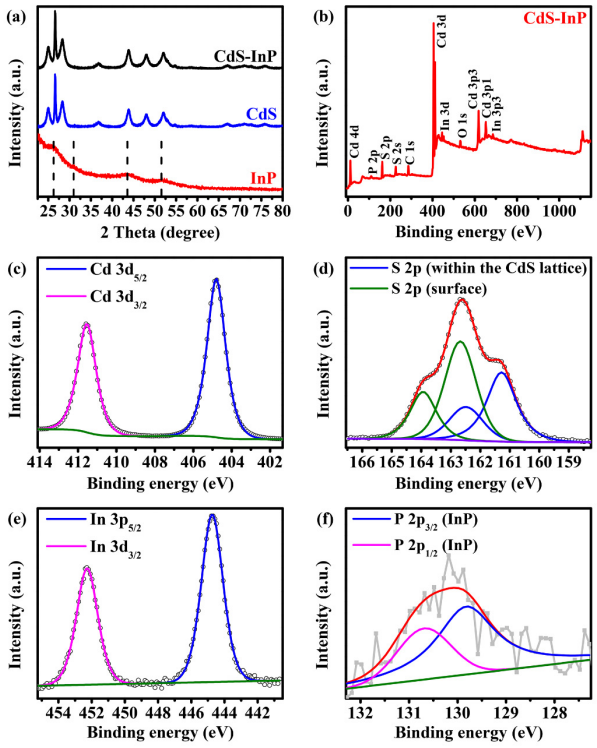

Figure 1. (a) XRD spectra of the InP QDs, CdS NRs and CdS-InP synthesized following the reference protocols described in the experimental section. (b) XPS survey spectrum of the as-prepared composite and high resolution XPS spectra of (c) Cd 3d, (d) S 2p, (e) In 2p and (f) P 2p regions.

10.1002/cctc.202000616

The crystal structures of the CdS NRs, InP QDs, and CdS-InP composites were analyzed via X-ray diffraction (XRD) analysis. The XRD patterns of the materials are shown in Figure 1a. The XRD pattern of CdS contained a series of diffraction peaks at 24.81°, 26.51°, 28.18°, 43.68°, 47.84°, and 51.82°, which were attributed to the (100), (002), (101), (110), (103), and (112) planes, respectively, of CdS in the pure hexagonal phase (JCPDS card no. 41-1049). The diffraction pattern of the bare InP QDs exhibited broad diffraction peaks at 26.3º, 43.6º, and 51.6º, which were in good agreement with the literature value.[46] Only CdS peaks were observed in the XRD patterns of the CdS-InP composites. No InP diffraction peaks appeared, which was due to the relatively low amount of InP relative to CdS and/or the low intensities of the InP diffraction peaks and overlap of the InP and CdS peaks.

The elemental surface chemistry of the CdS-InP was examined via XPS spectroscopy. The XPS survey spectrum (Figure 1b) of the CdS-InP composite contained peaks that were attributed to Cd, S, In, and P elements. The peaks of O 1s and C 1s, associated with the oxidized surface layer and oleylamine, were detected. The peaks located at 404.8 eV ($3d_{5/2}$) and 411.5 eV ($3d_{3/2}$) in the high-resolution XPS spectrum of Cd 3d (Figure 1c) were characteristic of Cd in the +2 oxidation state. Interestingly, the S 2p spectrum exhibited two doublets signals (Figure 1d). The first doublet, S $2p_{3/2}$ (162.7 eV) and S $2p_{1/2}$ (163.9 eV), was assigned to sulfur (S^{2-}) on the surface exposed to the more electronegative environment near InP, whereas the second component with S 2p spin-orbit splitting of ~1.2 eV (S $2p_{3/2}$ binding energy = 161.3 eV) corresponded to S^{2-} in the CdS lattice.[53,54] The In $3d_{5/2}$ and In $3d_{3/2}$ peaks appeared at 444.7 eV and 452.3 eV, respectively (Figure 1e). The high-resolution P 2p spectrum (Figure 1f) contained two contributions. The $2p_{1/2}$ and $2p_{3/2}$ peaks were found at respectively 130.7 eV and 129.8 eV, implying the presence of the phosphide (P^{3-}).[55,56] Relative to peaks in the XPS spectrum of pure InP (Figure S4), peaks in the XPS spectra of In and P in the CdS-InP composite were shifted slightly due to the modified chemical environment.

The morphology of the CdS-InP composites was investigated via transmission electron microscopy (TEM) (Figure 2) and energy dispersive X-ray spectral (EDS) mapping (Figure S3). Figure 2a shows a trace amount of InP QDs deposited onto CdS NRS. The high-resolution TEM (HRTEM) image of the composite (Figure 2b) clearly demonstrated two lattice spacings of 0.33 nm and 0.34 nm, which were assigned to CdS,[57] and InP,[47] respectively. The elemental compositions determined through EDS mapping (Figure S3) evidenced the distribution of InP on CdS.

The UV-visible spectroscopy was performed to study the optical properties of the InP QDs, the CdS NRs, and the composites (Figure 3a, b). The absorption spectrum of InP QDs in $CHCl_3$ contained a peak at 525 nm. This was close to the band edge position of bare CdS (~520 nm) and corresponded to intrinsic bandgap absorption by the CdS NRs.[58] Combining the CdS NRs and InP QDs did not alter the band structure of CdS. Rather, the InP QDs enhanced the absorption because of the similar absorption in the range from 500 to 550 nm. The more efficient utilization of visible light by the as-synthesized nanocomposites led to an increase in photocatalytic efficiency. The bandgap energy of the InP QDs was calculated using Tauc's method and found to be 2.20 eV. The estimated bandgap of the CdS semiconductor was 2.34 eV, which was consistent with the reported value [59].

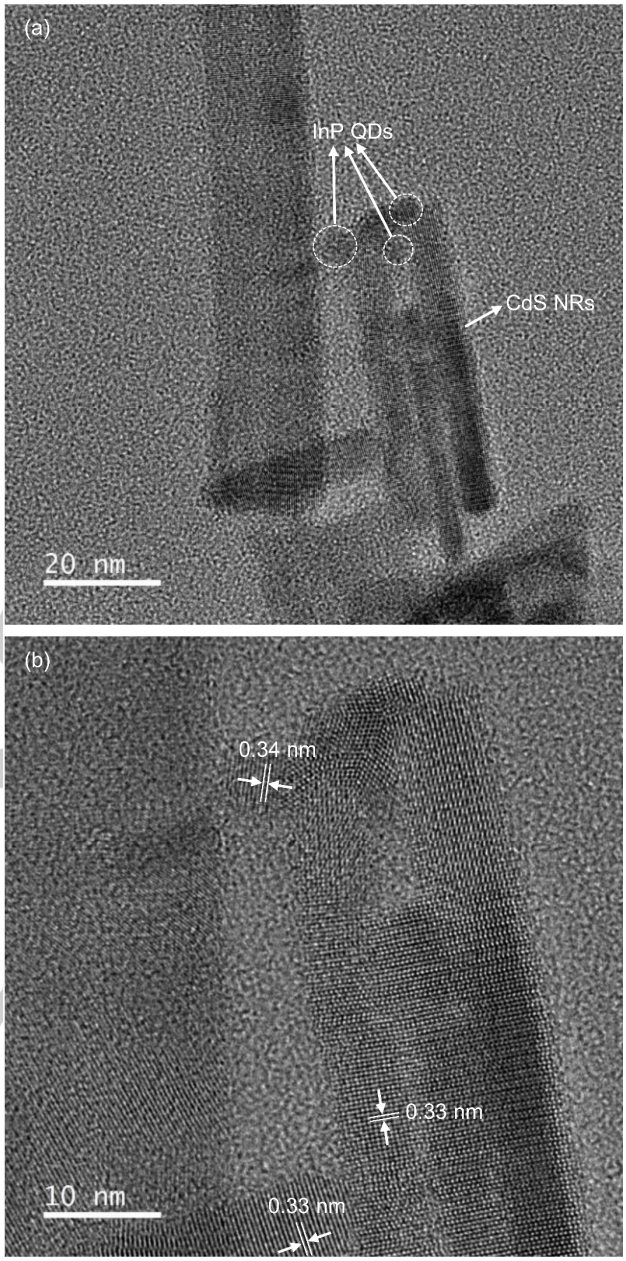

Figure 2. (a) TEM and (b) HR-TEM images of CdS-InP nanocomposites.

Photoluminescence (PL) emission spectroscopy is a useful technique for examining the trapping and charge recombination efficiencies of bare CdS and the related composites. The PL spectra of CdS and CdS-InP were recorded at an excitation wavelength of 380 nm at room temperature (Figure 4a). The rapid recombination of photogenerated charge carriers within the CdS nanorods generated a strong PL peak with band-edge emission appearing at ~520 nm.[28] In contrast, the lower peak intensity in the spectrum of as-prepared composites indicated the fast transfer of photoinduced electrons along with the suppression of charge carrier recombination, leading to enhancing photocatalytic activity.

10.1002/cctc.202000616

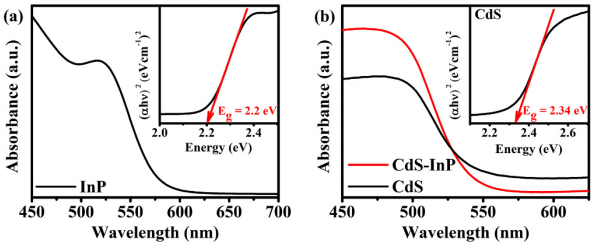

Figure 3. (a) UV-Visible absorption spectrum of InP QDs. (b) UV/Vis diffuse reflectance spectra of the CdS NRs and the related composite (b). Tauc plots of InP QDs and CdS NRs are inset into two panels (a) and (b), respectively to determine the band-gap energy

The dynamics of interfacial charge separation of as-synthesized materials were photoelectrochemically examined under simulated sunlight using a potentiostat and indium tin oxide (ITO) working electrodes coated with CdS and the CdS-InP nanocomposites. The time-dependent photocurrent responses of the bare CdS nanostructures and the nanocomposite (Figure 4b) were recorded over 360 seconds of 30 s on/off irradiation cycles. The CdS-InP nanocomposite generated a stronger photocurrent than the bare CdS nanorods, indicating that the separation of photoexcited electrons and holes was more efficient in the CdS-InP nanocomposite. The repeatability and stability of the photocurrent response over several on-off cycles demonstrated that the presence of InP on CdS NRs can prevent the photocorrosion. Photoelectrochemical (PEC) analysis confirmed that the InP QDs enhanced the photocatalytic activity of the CdS nanostructures. The semicircle in the Nyquist plot of the ITO electrode coated with CdS-InP was smaller in diameter than the semicircle in the Nyquist plot of CdS under simulated solar light (Figure 4c). This suggested that InP facilitated the migration of charge carriers from the InP QDs to the CdS NRs and other components of the reaction system.

The photocatalytic activities of the synthesized materials were examined by using TEOA as a sacrificial agent under simulated solar light (AM 1.5 G). During the photocatalytic reduction of CO_2, CO was generated as the major product. In detail, the blank experiments were performed for ensuring that light, TEOA, CO_2, and composites are the integral parts of CO_2 photoreduction systems (Figure S6a). Especially, the performance of the system in the Ar atmosphere was lower than that in the normal condition owing to the lower pH of the reaction mixture in the CO_2 atmosphere. The effect of the InP weight percentage in the InP-CdS nanocomposites on CO evolution is displayed in Figure 4d. The high recombination rate of as-synthesized CdS nanostructures resulted in very low solar-driven photocatalytic CO evolution rates of 287 μmol g^{-1} after 190 minutes of irradiation and approximately 400 μmol g^{-1} after 390 minutes. The coexistence of InP and CdS had a beneficial impact on the CO production rate. The CO generation rate of the composite containing 5.0 wt% InP reached a maximum of 216 μmol h^{-1} g^{-1} during the first three hours. The CO evolution rate under the higher InP loadings was lower. Excessive loading with InP covered active sites of CdS and hindered photocatalytic activity. The external quantum efficiency (EQE) of the optimized CdS-InP nanocomposite under visible light filtered through a 425 nm bandpass filter was estimated to be 0.44% during the first three hours of irradiation. The EQE then remained constant up to 6.5 hours of irradiation.

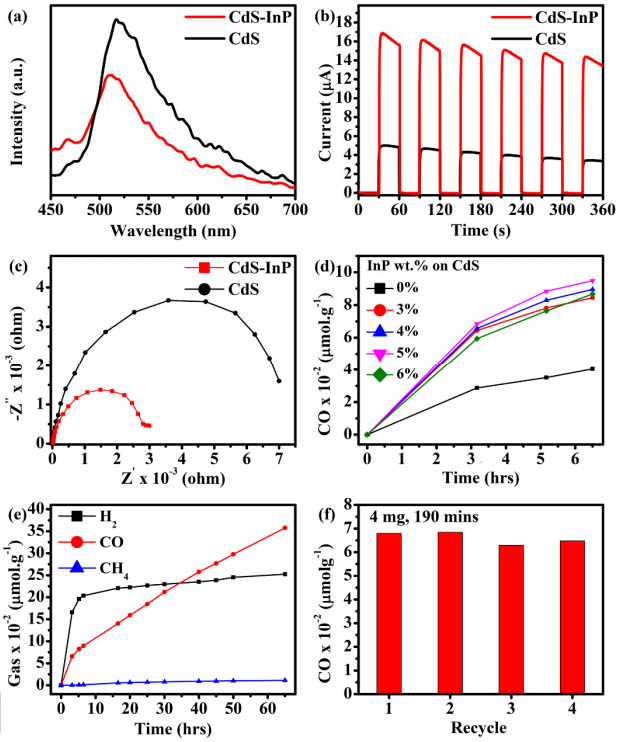

Figure 4. (a) PL spectra, (b) Transient photocurrent, and (c) Impedance measurements of pristine CdS and CdS-InP nanostructures. (d) Effect of InP QDs loading ratio on CdS NRs, (d) Long-term stability, and (f) Recyclability of CdS-5% InP with 4 mg of catalyst dispersed in 15 mL of 33.3 vol% aqueous TEOA solution under simulated solar light irradiation.

A Long-term photocatalysis experiment was performed with the optimized composite for up to 65 hours, as shown in Figure 4e. The CO yield increased with respect to the irradiation time while hydrogen evolution was suppressed after 5 hours and its rate rose slightly with increasing time. We concluded that CO_2 intermediates accumulated on the surface over time, which inhibited the adsorption of water and limited the water reduction process.[60] Furthermore, The pH of the solution increased during the photocatalysis experiment. This increased the solubility of CO_2 and affected positively photoreduction of CO_2.[61] The cycling experiments highlighted the stability and reusability of catalysts (Figure 4f). The optimized composite was reused after entirely recovering the photocatalyst particles from the reaction via centrifugation, washing with ethanol, and drying. It retained the activity after four recycling tests. In the case of evacuating for 3 hours and filling the reactor with CO_2 for 1 hour, there was a decrease in efficiency to nearly 50% in the second run (Figure S6c). The adsorption of the intermediates on the material surface in the first cycle hampered the interaction of reactants with the catalyst particles.

5% CdS-InP was collected after 6.5 hours of photocatalytic reaction to further examine the change of the photocatalyst. The used composite sample was characterized by means of XPS and TEM images. Both XPS spectra (Figure S7) and TEM images (Figure S8, 9) illustrated the presence of InP QDs on CdS surfaces, firmly suggesting the photostability of the composites. There was no change in the high resolution XPS spectrum in In 3d region, while the deconvolution of the P 2p signals was complicated by the low intensity of P peaks.

We used a wide variety of solvents for the optimized composite photo-experiments, which revealed the vital role of water in CO_2 conversion. The photocatalytic efficiency of the reaction system was generally better in the presence of water, which acted as a hydrogen source. The highest activity was observed in water (Figure S6d). The second position was MeCN/water, followed by DMF/water. To the best of our knowledge, lower activity in organic solvents was due to phase separation.[62,63] The influence of the scavenger concentration on the photocatalytic performance of the optimized composite was investigated. These results are shown in Figure S6e. The gas evolution rate was initially proportional to the TEOA concentration, which ranged up to 5 mL in a 15 mL reaction solution. The maximum CO production rate was 216 μmol h^{-1} g^{-1}. The intermediate formation was more pronounced at high TEOA concentrations, which reduced photocatalytic efficiency.[64] The photocatalytic activity of the optimized CdS-InP composite catalyst in 15 ml of the reaction solution was profoundly dependent on the amount added (3 – 5 mg), as illustrated in Figure S6f. Although the selectivity for CO (~30%) was roughly the same regardless of the amount of catalyst added, the rates of CO production differed. The CO evolution rates with 3, 4, and 5 mg of the photocatalyst were 200, 216, and 149 μmol h^{-1} g^{-1}, respectively. A larger quantity of the catalyst had a shielding effect on the suspended nanocomposites, which resulted in a lower CO evolution rate.

Mott-Schottky (MS) measurements were carried out to further research the CO_2 photoreduction mechanism of as-synthesized materials (Figure S10). The flat band potentials (V_{FB}) of CdS and the CdS-InP nanocomposite in the MS measurements were -0.847 V and −0.919 V vs. $E_{Ag/AgCl}$, respectively, at the frequencies of 0.5 and 0.1 kHz. Following potential conversion from the Ag/AgCl reference to NHE, the V_{FB} values were -0.650 V and -0.722 V vs. NHE.[65] The conduction band potential (E_{CB}) of the CdS NRs with a bandgap of 2.34 eV was −0.65 V vs. NHE and the E_{CB} of the InP QDs with a bandgap of 2.20 eV equaled −0.72 V, in line with the report,[47] because of the closeness between the conduction band potential of an n-type semiconductor and the flat band potential.[66] Therefore, the valence band potential (E_{VB}) values of CdS NRs and InP QDs are estimated to be 1.69 V and 1.48 V vs. NHE, respectively.

Based on PL, PEC, and MS measurements, a plausible mechanism of the solar-driven CO_2 reduction using the CdS-InP nanocomposites and TEOA as a hole scavenger is depicted in Scheme 2. The excitations of the CdS and InP in the CdS-InP nanocomposites by solar light generated electron-hole pairs. The electrons were located in the conduction bands (CBs), and the holes were in the valence bands (VBs). Since CdS-InP composites were type II heterostructures, the photogenerated electrons migrated directly from the CB of InP to the CB of CdS. The photogenerated holes in the VB of CdS traveled in the opposite direction to the VB of InP. Consequently, the photoinduced electrons in the CB of CdS reduced CO_2 on the surface into CO. Meanwhile, the holes in the VB of InP were consumed by the sacrificial electron donor (TEOA). The InP QDs enabled the effective separation of the photogenerated charge carriers and enhanced the harvesting of solar radiation, which was supported by the UV-Vis measurements. Moreover, the conduction band potentials of CdS and InP were very similar, which allowed the rapid migration of electrons from InP to CdS.

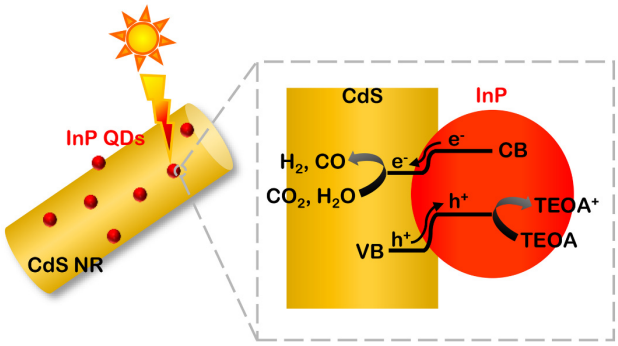

Scheme 2. Schematic representation of the reaction mechanism for photocatalytic CO_2 reduction of CdS-InP composite.

Conclusion

A simple and inexpensive process for the preparations of pure InP QDs, CdS NRs, and CdS-InP nanocomposites was successfully developed. The CdS-InP composites demonstrated enhanced sunlight-driven photocatalytic CO_2 reduction activity in water relative to bare CdS. This was due to the improved separation of photogenerated electron-hole pairs and better absorption capability in the 500–550 nm range. The performance of the optimized composite was investigated in different solvents, indicating the important role of water in CO_2 photoreduction. In addition, the suppression of H_2 evolution after five hours of irradiation in the long-term photocatalysis experiment resulted in enhanced CO selectivity during CO_2 reduction. Considering each of these factors, the InP-CdS nanocomposites are promising candidates for harvesting solar energy, photochemical conversion, and storage.

Experimental Section

Chemicals: Indium(III) chloride (99.999%), Oleylamine (70%), Tris(diethylamino)phosphine (97%) were purchased from Sigma-Aldrich. Acetonitrile (ACN), Cadmium acetate dihydrate ($Cd(CH_3COO)_2{\cdot}2H2O$), Chloroform, Ethanol, N,N-Dimethylformamide (DMF), Triethanolamine and Zinc(II) chloride were purchased from Daejung Chemicals & Metals Co. Ltd., Korea. Thiourea (NH_2CSNH_2) was obtained from Kanto Chemical Co. Inc., Japan.

Synthesis of InP QDs: Indium phosphide (InP) was prepared from indium chloride and tris (diethylamino)phosphine in the presence of $ZnCl_2$, according to the method reported with some modifications.[46] A suspension of 100 mg (0.45 mmol) indium(III) chloride, 300 mg (2.2 mmol) zinc(II) chloride, and 3.0 ml toluene in technical oleylamine (5.0 mL) was stirred and degassed at ambient temperature for 30 minutes. The mixture was then stirred at 80 °C for 30 minutes, at 120 °C for 30 minutes, and at 135 °C for 30 minutes. Once the temperature reached 180 °C, a volume of 0.45 mL (1.6 mmol) of tris(diethylamino)phosphine (phosphorus:indium ratio = 3.6:1) was quickly injected into the mixture under an inert atmosphere. The temperature of the mixture was held at 180 °C for 30 minutes. When the reaction was complete, the mixture was allowed to cool to room temperature. The raw InP QDs were obtained by adding 20.0 mL ethanol, centrifuging and discarding the supernatant. The samples were purified twice using 10.0 mL chloroform ($CHCl_3$) as the solvent and 15.0 mL ethanol as the nonsolvent and washing them again with ethanol. Finally, the QDs were added to 20.0 mL of $CHCl_3$ and centrifuged to remove the

insoluble impurities. The QD solution was stored in the absence of free oxygen and moisture.

To determine the mass concentration of InP QDs, the exact volume of the solution was taken, and then the residue was weighed after evaporation of $CHCl_3$ under reduced pressure at room temperature. It was estimated that 1 mL mixture contained about 3 mg InP QDs.

Synthesis of cadmium sulfide nanorods: Cadmium sulfide nanorods (CdS NRs) were prepared using the solvothermal technique. A mixture of 1335.5 mg (5 mmol) cadmium acetate ($Cd(CH_3COO)_2 \cdot 2H_2O$) and 381.4 mg (5 mmol) thiourea (CH_4N_2S) was suspended in the solvent of ethylenediamine (60.0 mL) under constant magnetic stirring for 30 minutes. The subsequent mixture was transferred to a Teflon-lined stainless-steel autoclave vessel of 100 mL capacity. The vessel was placed in a 160 °C hot air oven and heated for 48 hours. The mixture after the reaction was cooled normally off to ambient temperature and obtained yellow solid precipitate. The precipitate was cleaned with de-ionized water and ethanol several times to eliminate the impurities, then dried at 80 °C for 12 hours.

Synthesis of InP QDs/CdS NRs composites: The CdS-InP composites were prepared using the wet impregnation method. 35.0 mg of CdS NRs were dispersed in 3.5 mL volumes of ethanol, and the mixtures were ultrasonicated for 15 minutes at room temperature. The requisite amounts of InP QDs in $CHCl_3$ were added to the mixtures, which were kept for ultrasonic treatment again for 15 minutes under an inert atmosphere. The solvent was evaporated under reduced pressure at room temperature to obtain CdS-InP composites, which were well kept in the absence of free oxygen and water moisture.

Characterization methods: To specify the crystal structures of the powder samples, Ultima IV X-ray diffractometer using Cu Kα radiation as the X-ray source was used. The crystal structure of InP QDs was determined using a SmartLab high-resolution X-ray diffractometer (Rigaku). The chemical states and elemental compositions of the samples were evaluated via X-ray photoelectron spectroscopy (XPS). Measurements were performed using a K-alpha system (ThermoScientific, USA) equipped with a monochromated Al K_α X-ray source (1,486.6 eV) operated at 36 W (12 kV, 3 mA). The C 1s at 284.8 eV was selected as the standard peak to calibrate the energy scale. Transmission electron microscopy (TEM) images and elemental maps were obtained using a JEM-200 TEM (JEOL, Japan) equipped with an energy dispersive X-ray spectrometer (EDS) at an accelerating voltage of 200 kV to characterize the microstructure properties. The UV-VIS absorption measurements were operated using a V-770 UV-VIS/NIR spectrophotometer. Photoluminescence (PL) spectra of the photocatalysts were recorded on a F-7000 fluorescence spectrometer (Hitachi, Japan) at ambient temperature. Inductively Coupled Plasma Optical Emission Spectrometer (OPTIMA 8300 ICP-OES) was employed to analyze the compositions of the samples. The mass ratios between In and Cd elements in different samples characterized by ICP-OES are shown in Table S1.

Photocatalytic activity: In a typical photocatalytic CO_2 reduction experiment, 4.00 mg of the catalyst was dispersed in 15.0 mL 2:1 (v/v) water/TEOA in a Pyrex flask at ambient temperature and atmospheric pressure. The flask was sealed with a silicone rubber septum and evacuated for 30 minutes. The reaction mixture was then purged for 1 h to saturate the solution. The photo-irradiation light source was a solar simulator equipped with a 150 W Xe lamp (Abet Technologies, USA) and an AM 1.5G filter. The output intensity was maintained at 1 sun (100 W m^{-2}) using a Model 15151 calibrated Si reference cell (ABET Technologies). An off-line Model 4900 gas chromatograph (Young Lin) and the Autochro-3000 software package were used for product analysis. Evolved hydrogen gas was detected using a thermal conductivity detector (TCD), while a flame ionization detector (FID) was used to detect CO and CH_4. Two independent measurements were performed to evaluate reproducibility. For recycling tests, 4 mg of used catalyst was collected by centrifugation, washed three times with ethanol (7 mL) and dried under reduced pressure at room temperature. Then, the operation was repeated as noted in CO_2 photoreduction experiments.

QE was determined under similar experimental conditions, except the 150 W Xe irradiation source was fitted with a 425 nm bandpass filter with an optical density of >4 in the rejection band and a slope factor of <1% at the adjusted intensity. The liquid level was ~16 cm from the lamp window, and a 21.24 cm^2 area was illuminated. The apparent quantum efficiency (QE) was calculated using the following equation:

$$\mathrm{QE}(\%) = \frac{(\text{Numbers of reacted electrons})}{(\text{Numbers of incident photons})} \times 100$$

$$= \frac{(n_{CO} \times 2 + n_{H_2} \times 2) \times N_A}{(\text{Numbers of incident photons})} \times 100$$

where n_{CO} and n_{H_2} represent moles of produced CO and H_2, respectively and N_A denotes Avogadro constant.

Photoelectrochemical measurements: Photoelectrochemical measurements were conducted using a CHI 617B electrochemical workstation in a standard three-electrode configuration. Pt wire was used as a counter electrode, and an Ag/AgCl electrode served as the reference electrode. The aqueous electrolyte solution contained 0.5 M Na_2SO_4. A 150 W Xe lamp equipped with an AM 1.5G filter was used for irradiation at an intensity of 1 sun. A uniform suspension containing 5.00 mg of an as-synthesized material, 450 µL ethanol, and 50 µL Nafion was spread onto glass pretreated with conductive indium tin oxide (ITO) and dried under reduced pressure. The transient photocurrent responses were measured at 0.0 V during the on-off cycling of the solar simulator. Electrochemical impedance spectroscopy (EIS) was performed at open circuit potential using an AC voltage of 5 mV. A standard potentiostat equipped with an impedance spectral analyzer was used to record Mott-Schottky plots at frequencies of 0.1 and 0.5 kHz over a potential range of −1.2 to 1.2 V in darkness. The measured potentials vs. Ag/AgCl were converted to the normal hydrogen electrode (NHE) scale according to $E_{NHE} = E_{Ag/AgCl} + 0.197$.

Acknowledgements

This work was supported by National Research Foundation of Korea (NRF) grants, funded by the Korean Government (MSIP) (2014R1A4A1001690 and 2016R1E1A1A01941978).

Keywords: CdS NRs Photocatalytic • Heterogeneous • InP QDs • Photocatalysis CO_2 Reduction • Suppression of H_2 Evolution

[1] P. Kumar, A. Kumar, B. Sreedhar, B. Sain, S. S. Ray, S. L. Jain, *Chem. Eur. J.* **2014**, *20*, 6154–6161.

[2] P. Kumar, A. Kumar, C. Joshi, R. Singh, S. Saran, S. L. Jain, *RSC Adv.* **2015**, *5*, 42414–42421.

[3] M. Wang, M. Shen, L. Zhang, J. Tian, X. Jin, Y. Zhou, J. Shi, *Carbon* **2017**, *120*, 23–31.

[4] C. Chen, T. Wu, H. Wu, H. Liu, Q. Qian, Z. Liu, G. Yang, B. Han, *Chem. Sci.* **2018**, *9*, 8890–8894.

[5] B. Su, L. Huang, Z. Xiong, Y. Yang, Y. Hou, Z. Ding, S. Wang, *J. Mater. Chem. A* **2019**, *7*, 26877–26883.

[6] M. Zhou, S. Wang, P. Yang, C. Huang, X. Wang, *ACS Catal.* **2018**, *8*, 4928–4936.

[7] Q. Gai, X. Zheng, W. Liu, Q. Dong, Y. Wang, R. Gao, S. Ren, *Int. J. Hydrogen Energy* **2019**, *44*, 27412–27420.

[8] H. Lee, D. A. Reddy, Y. Kim, S. Y. Chun, R. Ma, D. P. Kumar, J. K. Song, T. K. Kim, *ACS Sustainable Chem. Eng.* **2018**, *6*, 16734–16743.

[9] S. Chen, L. W. Wang, *Chem. Mater.* **2012**, *24*, 3659–3666.

[10] M. J. Berr, P. Wagner, S. Fischbach, A. Vaneski, J. Schneider, A. S. Susha, A. L. Rogach, F. Jäckel, J. Feldmann, *Appl. Phys. Lett.* **2012**, *100*, 223903.

[11] D. A. Reddy, E. H. Kim, M. Gopannagari, Y. Kim, D. P. Kumar, T. K. Kim, *Appl. Catal. B* **2019**, *241*, 491–498.
[12] S. Hong, D. P. Kumar, E. H. Kim, H. Park, M. Gopannagari, D. A. Reddy, T. K. Kim, *J. Mater. Chem. A* **2017**, *5*, 20851–20859.
[13] S. Hong, D. P. Kumar, D. A. Reddy, J. Choi, T. K. Kim, *Appl. Surf. Sci.* **2017**, *396*, 421–429.
[14] Z. Zhu, Y. Han, C. Chen, Z. Ding, J. Long, Y. Hou, *ChemCatChem* **2018**, *10*, 1627–1634.
[15] Z. Zhu, J. Qin, M. Jiang, Z. Ding, Y. Hou, *Appl. Surf. Sci.* **2017**, *391*, 572–579.
[16] P. Zhang, S. Wang, B. Y. Guan, X. W. D. Lou, *Energy Environ. Sci.* **2019**, *12*, 164–168.
[17] S. Ijaz, M. F. Ehsan, M. N. Ashiq, N. Karamat, T. He, *Appl. Surf. Sci.* **2016**, *390*, 550–559.
[18] A. A. Beigi, S. Fatemi, Z. Salehi, *J. CO2 Util.* **2014**, *7*, 23–29.
[19] J. Jin, J. Yu, D. Guo, C. Cui, W. Ho, *Small* **2015**, *11*, 5262–5271.
[20] K. M. Cho, K. H. Kim, K. Park, C. Kim, S. Kim, A. Al-Saggaf, I. Gereige, H. T. Jung, *ACS Catal.* **2017**, *7*, 7064–7069.
[21] J. Yu, J. Jin, B. Cheng, M. Jaroniec, *J. Mater. Chem. A* **2014**, *2*, 3407-3416.
[22] X. Li, J. Chen, H. Li, J. Li, Y. Xu, Y. Liu, J. Zhou, *J. Nat. Gas Chem.* **2011**, *20*, 413–417.
[23] S. Wang, X. Wang, *Appl. Catal., B* **2015**, *162*, 494–500.
[24] Y. Liu, L. Deng, J. Sheng, F. Tang, K. Zeng, L. Wang, K. Liang, H. Hu, Y. N. Liu, *Appl. Surf. Sci.* **2019**, *498*, 143899.
[25] S. Cao, Y. Chen, H. Wang, J. Chen, X. Shi, H. Li, P. Cheng, X. Liu, M. Liu, L. Piao, *Joule* **2018**, *2*, 549–557.
[26] Z. C. Fu, R. C. Xu, J. T. Moore, F. Liang, X. C. Nie, C. Mi, J. Mo, Y. Xu, Q. Q. Xu, Z. Yang, et al., *Chem. Eur. J.* **2018**, *24*, 4273–4278.
[27] Y. He, R. Cui, C. Gao, J. Zhang, X. Li, *Mol. Catal.* **2019**, *469*, 161–166.
[28] Y. Dong, L. Kong, G. Wang, P. Jiang, N. Zhao, H. Zhang, *Appl. Catal. B* **2017**, *211*, 245–251.
[29] J. Wang, P. Wang, J. Hou, J. Qian, C. Wang, Y. Ao, *Catal. Sci. Technol.* **2018**, *8*, 5406–5415.
[30] Z. Pan, R. Wang, J. Li, S. Iqbal, W. Liu, K. Zhou, *Int. J. Hydrogen Energy* **2018**, *43*, 5337–5345.
[31] S. Riyajuddin, S. K. T. Aziz, S. Kumar, G. D. Nessim, K. Ghosh, *ChemCatChem* **2020**, *12*, 1394–1402.
[32] Y. Li, Z. Jin, H. Liu, H. Wang, Y. Zhang, G. Wang, *J. Colloid Interface Sci.* **2019**, *541*, 287–299.
[33] Q. Liu, J. Xing, Z. Jiang, X. Jiang, Y. Wang, J. Zhao, *Nanoscale* **2020**, *12, 6776–6784*.
[34] D. C. Gary, S. E. Flowers, W. Kaminsky, A. Petrone, X. Li, B. M. Cossairt, *J. Am. Chem. Soc.* **2016**, *138*, 1510–1513.
[35] H. Li, C. Jia, X. Meng, H. Li, *Front. Chem.* **2019**, *6*, *652*.
[36] P. Liu, J. A. Rodriguez, T. Asakura, J. Gomes, K. Nakamura, *J. Phys. Chem. B* **2005**, *109*, 4575–4583.
[37] Z. Fang, L. Peng, Y. Qian, X. Zhang, Y. Xie, J. J. Cha, G. Yu, *J. Am. Chem. Soc.* **2018**, *140*, 5241–5247.
[38] F. J. Reid, R. K. Willardson, *Int. J. Electron.* **1958**, *5*, 54–61.
[39] B. Zhao, Y. Huang, D. Liu, Y. Yu, B. Zhang, *Sci. China Chem.* **2020**, *63*, 28–34.
[40] Y. H. Won, O. Cho, T. Kim, D. Y. Chung, T. Kim, H. Chung, H. Jang, J. Lee, D. Kim, E. Jang, *Nature* **2019**, *575*, 634–638.
[41] C. F. Lai, Y. C. Tien, H. C. Tong, C. Z. Zhong, Y. C. Lee, *RSC Adv.* **2018**, *8*, 35966–35972.
[42] Q. Zhao, A. Hazarika, X. Chen, S. P. Harvey, B. W. Larson, G. R. Teeter, J. Liu, T. Song, C. Xiao, L. Shaw, et al., *Nat. Commun.* **2019**, *10*, 1–8.
[43] Y. Zheng, Y. Chen, B. Gao, J. Chen, Z. Du, B. Lin, *Mater. Lett.* **2019**, *254*, 81–84.
[44] X. B. Li, Z. J. Li, Y. J. Gao, Q. Y. Meng, S. Yu, R. G. Weiss, C. H. Tung, L. Z. Wu, *Angew. Chem. Int. Ed.* **2014**, *53*, 2085–2089.
[45] C. Wang, R. L. Thompson, J. Baltrus, C. Matranga, *J. Phys. Chem. Lett.* **2010**, *1*, 48–53.
[46] M. D. Tessier, D. Dupont, K. De Nolf, J. De Roo, Z. Hens, *Chem. Mater.* **2015**, *27*, 4893–4898.
[47] S. Yu, X. Fan, X. Wang, J. Li, Q. Zhang, A. Xia, S. Wei, L. Wu, Y. Zhou, G. R. Patzke, *Nat. Commun.* **2018**, *9*, 1–10.
[48] K. Wu, N. Song, Z. Liu, H. Zhu, W. Rodríguez-Córdoba, T. Lian, *J. Phys. Chem. A* **2013**, *117*, 7561–7570.
[49] R. Toufanian, A. Piryatinski, A. H. Mahler, R. Iyer, J. A. Hollingsworth, A. M. Dennis, *Front. Chem.* **2018**, *6*, 567.
[50] A. Buffard, S. Dreyfuss, B. Nadal, H. Heuclin, X. Xu, G. Patriarche, N. Mézailles, B. Dubertret, *Chem. Mater.* **2016**, *28*, 5925–5934.
[51] M. D. Tessier, K. De Nolf, D. Dupont, D. Sinnaeve, J. De Roo, Z. Hens, *J. Am. Chem. Soc.* **2016**, *138*, 5923–5929.
[52] M. E. Mundy, D. Ung, N. L. Lai, E. P. Jahrman, G. T. Seidler, B. M. Cossairt, *Chem. Mater.* **2018**, *30*, 5373–5379.
[53] T. Berestok, P. Guardia, J. B. Portals, S. Estradé, J. Llorca, F. Peiró, A. Cabot, S. L. Brock, *Langmuir* **2018**, *34*, 6470–6479.
[54] H. Li, Z. Yuan, C. Bittencourt, X. Li, W. Li, M. Chen, W. Li, R. Snyders, *J. Environ. Chem. Eng.* **2019**, *7*, 102910.
[55] H. Virieux, M. Le Troedec, A. Cros-Gagneux, W. S. Ojo, F. Delpech, C. Nayral, H. Martinez, B. Chaudret, *J. Am. Chem. Soc.* **2012**, *134*, 19701–19708.
[56] D. A. Granada-Ramirez, J. S. Arias-Cerón, M. L. Gómez-Herrera, J. P. Luna-Arias, M. Pérez-González, S. A. Tomás, P. Rodríguez-Fragoso, J. G. Mendoza-Alvarez, *J. Mater. Sci. Mater. Electron.* **2019**, *30*, 4885–4894.
[57] D. P. Kumar, M. I. Song, S. Hong, E. H. Kim, M. Gopannagari, D. A. Reddy, T. K. Kim, *ACS Sustainable Chem. Eng.* **2017**, *5*, 7651–7658.
[58] M. Zhang, H. Lin, J. Cao, X. Guo, S. Chen, *Chem. Eng. J.* **2017**, *321*, 484–494.
[59] M. Gopannagari, D. P. Kumar, D. A. Reddy, S. Hong, M. I. Song, T. K. Kim, *J. Catal.* **2017**, *351*, 153–160.
[60] Y. Lan, Y. Xie, J. Chen, Z. Hu, D. Cui, *Chem. Commun.* **2019**, *55*, 8068–8071.
[61] S. Liu, Z. Zhao, Z. Wang, *Photochem. Photobiol. Sci.* **2007**, *6*, 695–700.
[62] S. Roy, E. Reisner, *Angew. Chem. Int. Ed.* **2019**, *58*, 12308–12312.
[63] J. Lin, R. Liao, J. Xu, *RSC Adv.* **2018**, *8*, 3798–3802.
[64] P. Bhavani, D. P. Kumar, S. Jeong, E. H. Kim, H. Park, S. Hong, M. Gopannagari, D. A. Reddy, J. K. Song, T. K. Kim, *Catal. Sci. Technol.* **2018**, *8*, 1880–1891.
[65] M. Gopannagari, D. P. Kumar, H. Park, E. H. Kim, P. Bhavani, D. A. Reddy, T. K. Kim, *Appl. Catal. B* **2018**, *236*, 294–303.
[66] Y. Zhang, Z. Jin, *Phys. Chem. Chem. Phys.* **2019**, *21*, 8326–8341.

10.1002/cctc.202000616

Entry for the Table of Contents

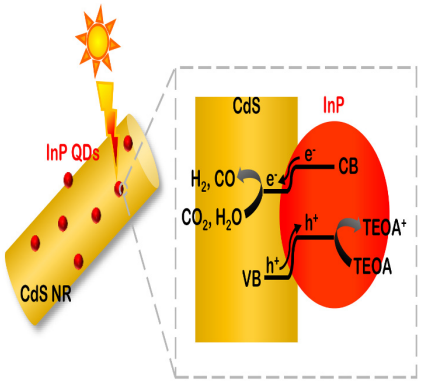

The simple and cost-effective synthesis of noble metal-free CdS-InP composites for high photocatalytic CO_2 conversion into CO in aqueous solution is demonstrated. These synthesized materials are the potential candidates for pouring efforts into research on solar energy harvesting applied to photochemical conversion and storage fields.